

Lithium Peroxide Surfaces and Point Defects: Relevance for Li-air Batteries

Maxwell D. Radin¹, Jill F. Rodriguez², Donald J. Siegel^{2,3,4}

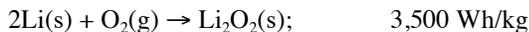
¹Dept. of Physics, ²Mechanical Engineering Dept., ³Applied Physics Program, ⁴Michigan Memorial Phoenix Energy Institute
University of Michigan, Ann Arbor, MI 48109-2133

Abstract

The ability to store electrical energy at high densities, high efficiencies, and with low costs is a cross-cutting issue that impacts a wide range of applications. Rechargeable lithium-air batteries are a newer form of energy storage with theoretical energy densities approximately an order of magnitude greater than today's lithium-ion batteries. However, despite this potential, Li-air technology remains at an early stage of development with many performance limitations yet to be addressed, including high overpotentials needed for recharging. We hypothesize that slow decomposition kinetics of the Li_2O_2 discharge phase contributes to the overpotential and resulting low efficiencies. Although cathode catalysts have been shown to modestly lower charging potentials, little is known about the rate-limiting steps involved in Li_2O_2 decomposition, or how these mechanisms are altered in the presence of catalysts. Towards the goal of identifying optimal catalysts, we apply state-of-the-art first principles atomistic simulations to elucidate equilibrium crystallite morphologies and defect mobilities in Li_2O_2 . We find that Li_2O_2 particles form as hexagonal prisms, with 37% of their surface area consisting of an oxygen-rich $\{0001\}$ phase and 63% a stoichiometric $\{1-100\}$ phase. The concentrations and diffusivities of all chemically-relevant intrinsic point defects in Li_2O_2 were evaluated; the dominant defect at atmospheric conditions is the negatively-charged lithium vacancy, with a free energy of formation of 0.47 eV. Assuming Li migration occurs via a vacancy mechanism, the diffusivity of lithium is predicted to be $\sim 10^{-20}$ m²/s. In contrast, oxygen is found to be essentially immobile. Since the Li diffusion length is considerably less than typical Li_2O_2 particle sizes observed in discharged cells, we conclude that slow mass transport in Li_2O_2 contributes to the high overpotentials observed during recharge.

Introduction

Many technologies stand to benefit from high capacity energy storage. Some prominent examples include battery powered electric vehicles (BEVs) and the penetration of renewable power sources (i.e., wind and solar) on the electrical grid. The state of the art rechargeable battery, Li-ion, has a cell level specific energy density of ~ 200 Wh/kg [1], which is inadequate for applications requiring large energy densities [2]. The Li-air battery is an alternative chemistry that uses atmospheric oxygen as a reactant, and may offer an order of magnitude increase in specific energy density [3, 4]. Li-air batteries are characterized by two possible reactions wherein the product phase is either a solid peroxide (Li_2O_2) or oxide (Li_2O):



(Here the mass of oxygen is included in the calculation of the specific energy density.) Abraham *et al.* were the first to demonstrate a prototype *rechargeable* Li-air battery consisting of a lithium metal anode and an air-breathing carbon cathode separated by a Li^+ conductive polymer electrolyte membrane [5]. Although Raman spectra indicated that the primary discharge product was Li_2O_2 [5], Li_2O has also been observed in other studies [6]. Later experiments confirmed that Li_2O_2 decomposes to Li and O_2 during recharge [7].

Despite growing interest in Li-air batteries [3-13], several challenges must be overcome in order to achieve commercial viability. These include: (i.) Low efficiencies caused by high overpotentials during charging; (ii.) Low rates of charge/discharge; (iii.) Poor capacity retention; and (iv.) Sensitivity to moisture in the air stream. Regarding efficiency, capacity retention, and current density, a small number of catalysts have been identified that can improve performance, including metals [10], metal oxides [12], and ceramic powder [13]. For example, Débart *et al.* found that Co_2O_3 improved capacity retention and lowered the charging potential by 800 mV in comparison to a system with no catalyst [12].

Additional experiments have shown that a combination of gold and platinum nanoparticles reduced the charging potential by 900 mV, thereby increasing efficiency from 57% to 73% [10]. Although these improvements are promising, the resulting efficiencies are still well short of the 90+% efficiency achieved in Li-ion batteries.

At a fundamental level, the performance of Li-air cells can be traced to atomic-scale processes related to the catalytic nucleation & growth (during discharge) and decomposition (recharge) of Li_2O_2 . However, to date there have been very few [8, 9, 11] atomistic modeling studies targeting Li-air materials or phenomena. For example, Hummelshøj *et al.* have proposed a mechanism for Li_2O_2 growth via adsorption [9]. Another computational study has suggested pathways by which gold and platinum surfaces facilitate O_2 reduction by lithium [8]. Seriani has calculated the thermodynamic stability

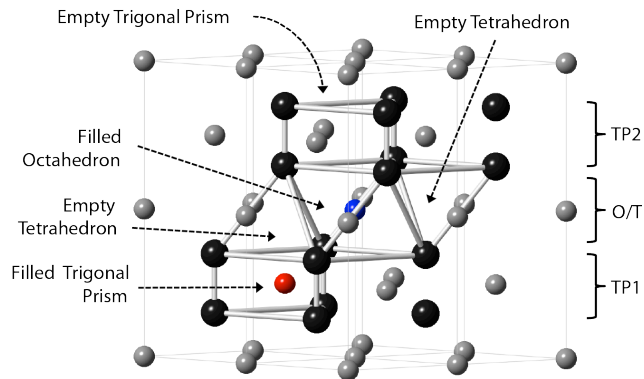


FIG. 1: (Color online) Crystal structure of Li_2O_2 depicted using a 2×2 supercell. Large black spheres represent oxygen atoms, small grey spheres represent Li atoms. The red and blue atoms indicate the positions of the two symmetry-distinct Li atoms, which are located either within trigonal prisms or octahedra, respectively. The layers are named according to the shape of the polyhedra formed by adjacent O atoms within that layer: TP1 = trigonal prism layer 1, O/T = octahedron/tetrahedron layer, TP2 = trigonal prism layer 2.

of Li_2O and Li_2O_2 nanoparticles [11]. We are not aware of any modeling of the Li-air recharge process and the associated decomposition of Li_2O_2 . Given the existence of conflicting experimental data [10, 12], and the appearance that catalyst development is progressing in an Edisonian fashion, it is clear that a more thorough understanding of rate-limiting mechanisms in the Li-air cathode would be highly beneficial.

Regarding surfaces of Li_2O_2 , surface properties are important because the discharge process in Li-air cells is believed to occur via the nucleation and growth of Li_2O_2 via surface adsorption. To understand the thermodynamics and kinetics of these processes, and their consequences for rate capabilities, it is important to identify the structure and chemical composition of the most commonly observed (i.e., most stable) surfaces. Reuter and Scheffler [14] have described a general first-principles thermodynamic approach for evaluating surface energies for different terminations of crystalline compounds as a function of temperature and pressure, and have demonstrated this approach on surfaces of RuO_2 . Seriani recently reported a study of surfaces and nanoparticles of Li_2O_2 and Li_2O [11]. In the present study, we expand on Seriani's work by calculating the surface free energies of Li_2O_2 for a much wider range of possible surface terminations. Combining these energies with the Wulff construction [25], we find that the equilibrium shape of Li_2O_2 crystallites is a hexagonal prism, 37% of whose surface area consists of an oxygen-rich $\{0001\}$ phase and 63% a stoichiometric $\{1-100\}$ phase.

Regarding bulk properties, we have also used density functional theory calculations to examine mass transport kinetics (i.e., self-diffusion) in Li_2O_2 . We speculate that slow mass transport within Li_2O_2 may limit its decomposition rate, and thus contribute to the high overpotentials observed upon charging of Li-air batteries. The catalytic decomposition of solid phases remains a highly active area of research, especially in the hydrogen storage community [15]. As it is well known that defects mediate bulk diffusion and mass transport [16], this suggests that they may impact the rate of Li_2O_2 decomposition. As a first step in elucidating decomposition mechanisms, we employ density functional theory to calculate formation energies for all chemically relevant intrinsic point defects in Li_2O_2 at experimentally relevant temperatures and pressures. Subsequently, the

migration energies along several crystallographic directions were evaluated for those defects exhibiting low formation energies. We find that negatively charged lithium vacancies are the dominant defect at atmospheric conditions, with a free energy of formation of 0.47 eV. In contrast, the most favorable oxygen-based defect is a neutral vacancy with a significantly higher formation energy (0.61 eV). Our results indicate that mass transport in Li_2O_2 is relatively slow and mediated by Li vacancies: The diffusivity D of lithium is calculated to be $D \sim 10^{-20}$ m²/s, while oxygen is found to be essentially immobile. These small diffusivities imply that slow mass transport within Li_2O_2 may contribute to the inefficiencies observed during recharge of Li-air cells.

Methods

First principles calculations were performed using a spin polarized version of the generalized gradient approximation [17] to density functional theory [18, 19], as implemented in the Vienna *ab initio* simulation package [20]. The core-valence electron interaction was treated using Blöchl's projector augmented wave method [21]. The valence states ($2s$ for Li, $2s2p$ for O, and $1s$ for H) were expanded in a plane-wave basis set up to a cutoff energy of 400 eV. Electronic state occupancies were determined with a Gaussian smearing of width 0.1 eV. Atomic relaxations were converged to within a force tolerance of 0.02 eV/Å. Vibrational contributions to free energy, when included, were calculated within the harmonic approximation [22]. The energies of surfaces and defects that alter the Li_2O_2 stoichiometry depend on the chemical potential of oxygen, μ_{O} . As done by others [14], we define O-rich and O-poor limits for μ_{O} to reflect the range of possible values. Since density functional theory is known to overbind the oxygen molecule, we use the experimental formation enthalpy of water to more accurately estimate the ground state energy of O_2 [8, 9].

To determine which Li_2O_2 surface terminations are the most stable, we calculated surface free energies for 22 distinct terminations amongst three surface planes: $\{0001\}$, $\{1-120\}$, and $\{1-100\}$. We determined each surface's free energy γ at the oxygen-rich and oxygen-poor limits according to the following expressions [14]:

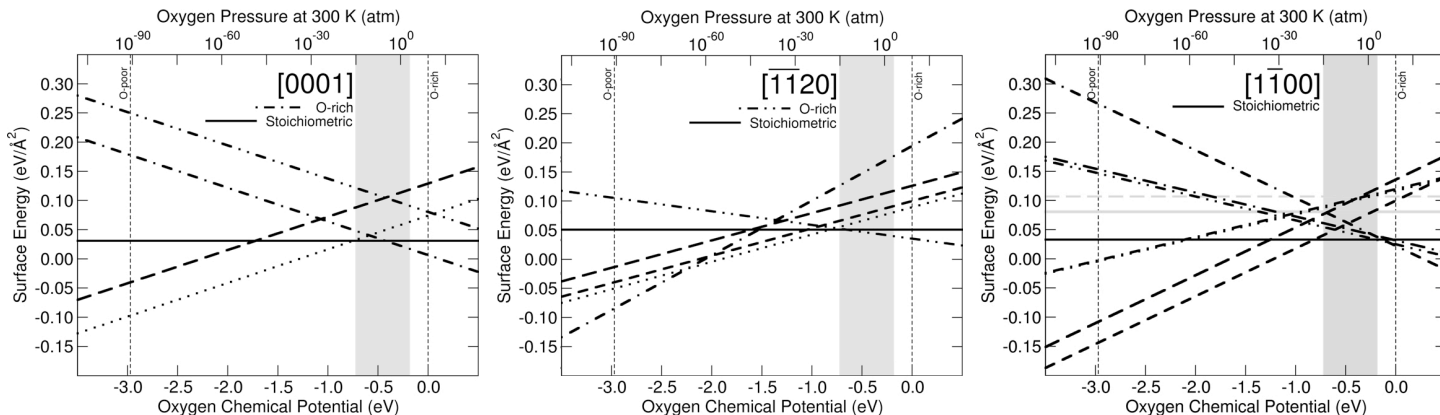


FIG. 2: Surface energies at $T = 300$ K for three low-index faces of Li_2O_2 as a function of oxygen chemical potential and surface termination. The gray box shows the experimentally-attainable pressure range $P_{\text{O}_2} = 10^{-15} - 10^3$ atm.

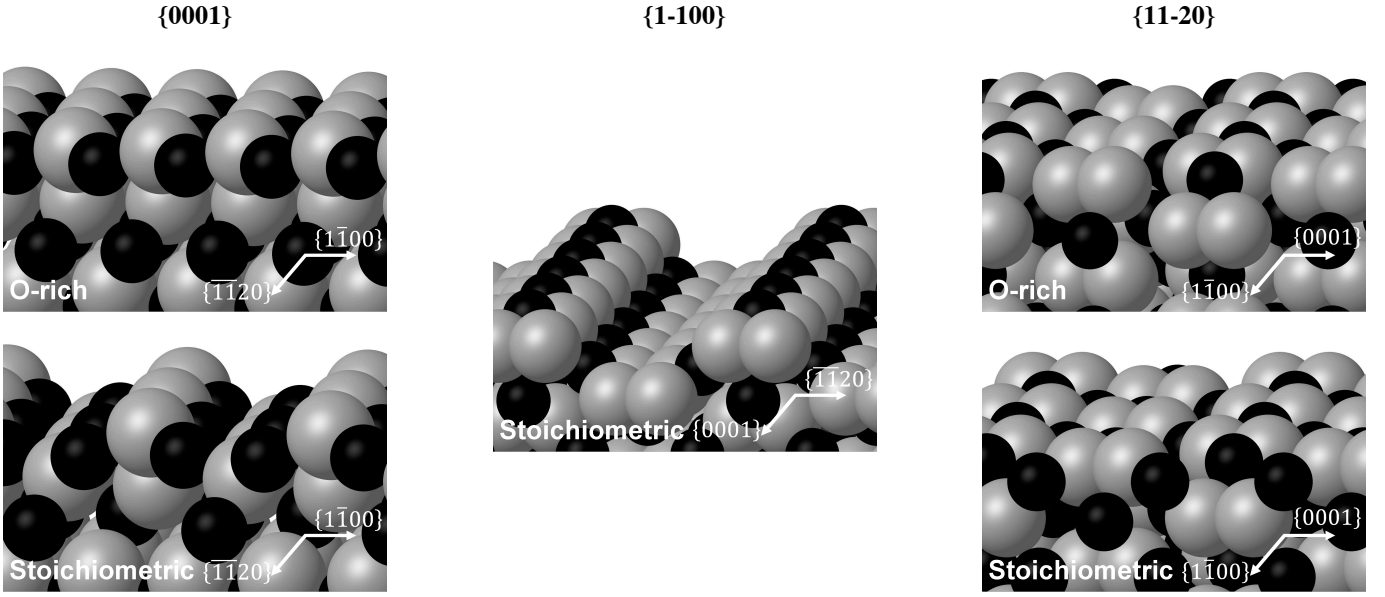


Fig. 3: Images of the lowest energy Li_2O_2 surface terminations in the experimentally accessible pressure regions from Fig. 2. Black atoms represent Li, gray atoms represent O.

$$\gamma^{O\text{-poor}} = \frac{1}{2A} [G^{\text{slab}} - \frac{1}{2}N_{\text{Li}}g_{\text{Li}_2\text{O}_2}^{\text{bulk}} + (N_{\text{Li}} - N_{\text{O}})(\frac{1}{2}g_{\text{Li}_2\text{O}_2}^{\text{bulk}} - g_{\text{Li}}^{\text{BCC}})]$$

$$\gamma^{O\text{-rich}} = \gamma^{O\text{-poor}} - \frac{1}{4A}(N_{\text{Li}} - N_{\text{O}})\Delta G_f$$

Here A represents the surface area, N_{Li} (N_{O}) is the number of Li (Oxygen) atoms in the computational cell, $g_{\text{Li}_2\text{O}_2}^{\text{bulk}}$ ($g_{\text{Li}}^{\text{bulk}}$) is the free energy of bulk Li_2O_2 (BCC Li), and ΔG_f is the Li_2O_2 formation free energy. Vibrational contributions to the free energies were included for all surfaces.

For bulk calculations, a $5 \times 5 \times 2$ supercell (400 atoms) was used to calculate defect formation energies in Li_2O_2 . For selected defects, vibrational contributions to free energy were calculated in a $3 \times 3 \times 2$ supercell. Cell shape and volume were held constant during these calculations. These cells were sampled with a $2 \times 2 \times 2$ Monkhorst-Pack k-point grid; we verified that defect formation energies were converged to within a few hundredths of an eV with respect to the supercell size. Charged defect calculations were performed using a compensating homogeneous background charge in order to prevent a divergence of the total energy. The nudged elastic band (NEB) method [23] was used for calculating migration barriers. Seven images were used in all NEB calculations; initial chains of states were generated via linear interpolation between the local minima at the beginning and end of the migration pathway.

The formation energy E_f of a defect in charge state q $E_f(X_q)$ was calculated as in Ref. [26]:

$$E_f(X_q) = E_0(X_q) - E_0(\text{bulk}) - \sum_i n_i \mu_i + q(\varepsilon_F + \varepsilon_V + \Delta V),$$

where $E_0(X_q)$ and $E_0(\text{bulk})$ are the energies of the defective and pristine supercells, n_i is the number of atoms of the i^{th} species in the defect, μ_i is the chemical potential of the i^{th} species, ε_F is the Fermi level, ε_V is the top of the valence band in the bulk,

and ΔV is the potential alignment correction. The concentration of defects [23] is then expressed as:

$$C(X_q) = \frac{D_X}{1 + e^{E_f(X_q)/kT}}.$$

Results and Discussion

A. Surfaces

Figure 1 shows the crystal structure of bulk Li_2O_2 , while Figure 2 shows the calculated surface energy for various $\{0001\}$, $\{1-100\}$, and $\{11-20\}$ Li_2O_2 surfaces as a function of oxygen chemical potential at $T = 300$ K. (Assuming a fixed temperature of 300mK, the chemical potential can be mapped onto a range of O_2 partial pressures, as shown on the top axis in each plot.) Those terminations having the lowest free energies for each surface plane within the experimentally accessible range of O_2 pressures – i.e., the most stable surfaces – are illustrated in Figure 3. The lowest energy $\{0001\}$ surfaces consist of an oxygen-rich surface (with $\gamma = 0.022$ eV/ \AA^2 at 1 atm, to be compared with 0.045 eV/ \AA^2 in Ref. [11]) and a stoichiometric surface ($\gamma = 0.031$ eV/ \AA^2 at 1 atm compared to 0.041 eV/ \AA^2 in Ref. [11]). We found the lowest energy $\{1-100\}$ surface to be the same one found by Hummelshøj *et al.* [9], with $\gamma = 0.033$ eV/ \AA^2 at 1 atm. The lowest energy $\{11-20\}$ surfaces were an oxygen-rich surface ($\gamma = 0.042$ eV/ \AA^2 at 1 atm compared to 0.043 eV/ \AA^2 in Ref. [11]) and a stoichiometric surface ($\gamma = 0.051$ eV/ \AA^2 at 1 atm compared to 0.052 eV/ \AA^2 in Ref. [11]).

Overall, the present surface energy values are systematically lower than those calculated by Seriani [11]. We believe that the difference in surface energies can be attributed to two differences in the calculation methodologies. First, it appears as though Ref. 11 did not explicitly include phonon contributions to the free energy, as done here; Secondly, Ref. 11 omitted the correction for the overbinding of O_2 molecules.

By combining the calculated surface free energies with

the Wulff construction, we predict that Li_2O_2 crystallites will assume the shape of a hexagonal prism, in agreement with the results found by Seriani [11]. 37.4% of the surface area of these particles will be comprised of the low-energy oxygen-rich $\{0001\}$ surface (top left panel, Fig. 3), with 62.6% consisting of a stoichiometric $\{1-100\}$ surface (middle panel, Fig. 3).

B. Bulk

As a first step towards understanding mass transport in bulk Li_2O_2 we have calculated the formation energies E_f for all chemically-relevant intrinsic (point) defects. The list of defect types considered includes: vacancies on either of the symmetry-distinct Li sites (denoted Li_v), oxygen vacancies (O_v), oxygen (O_i) or lithium (Li_i) interstitials in several different locations, and oxygen di-vacancies wherein an entire O_2 unit was removed from the supercell (O_{2v}). Interstitial sites examined include the center of a tetrahedron, the center of an empty triangular prism, the center of a face shared by two triangular prisms, the center of a face shared by an empty triangular prism and an octahedron (i.e. on the boundary between TP and O/T layer, Fig. 1), a face shared by an octahedron and a tetrahedron, and sites off-center of empty trigonal prisms. Neutral, positive, and negative ($q = 0; \pm 1$) charge states were examined for each defect type.

Figure 4 summarizes the calculated formation energies of all defects as a function of the Fermi level and oxygen chemical potential, μ_{O} . Here the value $\varepsilon_F = 0$ corresponds to the top of the valence band, with the maximum value $\varepsilon_F = 2.0$ eV set to our calculated value for the band gap/bottom of the conduction band. We consider three cases for μ_{O} : the conventional O-rich and O-poor limits, and atmospheric conditions wherein the energy per oxygen atom is set equal to that in gas-phase O_2 at $T = 300$ K and $P = 0.2$ atm.

Given calculated values for the formation energies, the next step in predicting defect concentrations is to determine the value of ε_F that satisfies the charge neutrality constraint [15] at a specified temperature, which we take as $T = 300$ K:

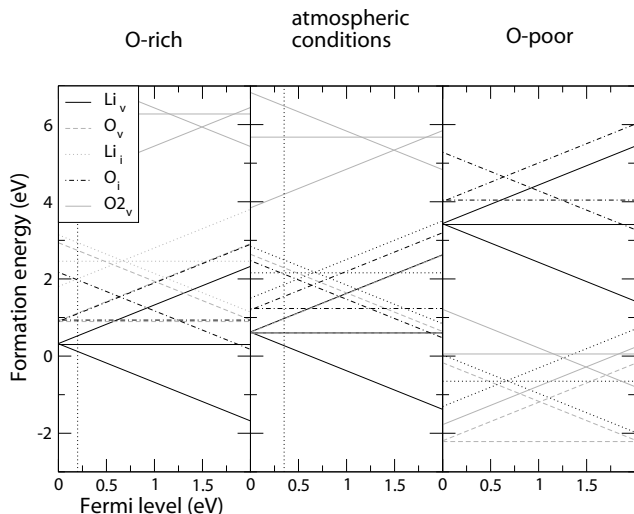


FIG. 4. Calculated formation energies (excluding vibrational contributions) of intrinsic defects in Li_2O_2 with charge states of 0 and ± 1 . The slope of the line indicates the charge state, and the vertical dotted line indicates the predicted Fermi level at 300 K.

	0	+1	-1
Atmospheric conditions			
$\text{Li}_v(\text{O/T})$	0.63 (0.65)	1.00 (0.93)	0.35 (0.54)
$\text{Li}_v(\text{TP})$	0.60 (0.59)	0.97 (0.88)	0.32 (0.47)
O_v	0.60 (0.61)	0.98 (0.76)	2.28
Li_i	2.16	1.98	2.52
O_i	1.23	1.61	2.15
O_{2v}	5.68	4.26	6.55

TABLE I. Calculated free energies of formation for various defects as a function of charge state ($q = -1, 0, 1$) at atmospheric conditions. Values shown in parenthesis include vibrational contributions.

$$p - n + \sum_i^{\text{defects}} q_i C_i = 0$$

Here q_i is the charge state of defect i , C_i is the concentration of that defect, p is the number density of holes in the valence band, and n is the number density of electrons in the conduction band. As we will later see, the Fermi level is close to the valence band, so we neglect the contribution from electrons in the conduction band. We can compute the number of holes in the valence band by assuming a constant density of states (estimated to be 5 states/unit cell eV from density of states calculations).

We find that in the O-rich environment $\varepsilon_F = 0.25$ eV whereas under atmospheric conditions $\varepsilon_F = 0.40$ eV. These values for ε_F are indicated by the vertical dotted lines in Figure 4. Under O-poor conditions, which at $T = 300$ K corresponds to a physically unrealizable O_2 partial pressure of 10^{-90} atm, the Fermi level is not physically meaningful because some defects have a negative formation energy.

At atmospheric conditions, the negative lithium vacancy has formation free energies (including vibrational contributions) of 0.47 eV at the TP site and 0.54 eV at the O/T site, as shown in Table 1. The total concentration of negative lithium vacancies is $0.4 \times 10^{17} \text{ cm}^{-3}$. The defects with the next lowest formation energies are neutral oxygen vacancies and neutral lithium vacancies, both with $E_f = 0.61$ eV and 0.59 eV.

Although in principle all defects contribute to diffusion, we consider only those defects having the lowest formation energies because these will be present in the highest

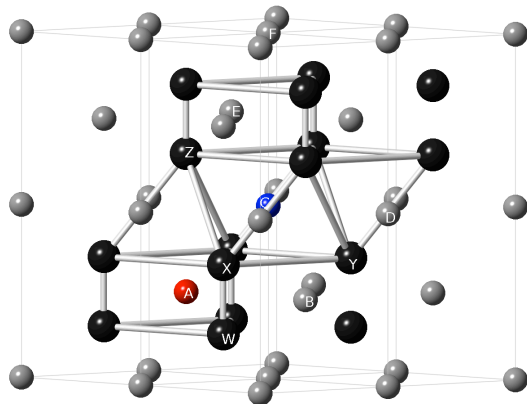


FIG. 5 (Color online) Labels for vacancy sites in the Li_2O_2 crystal

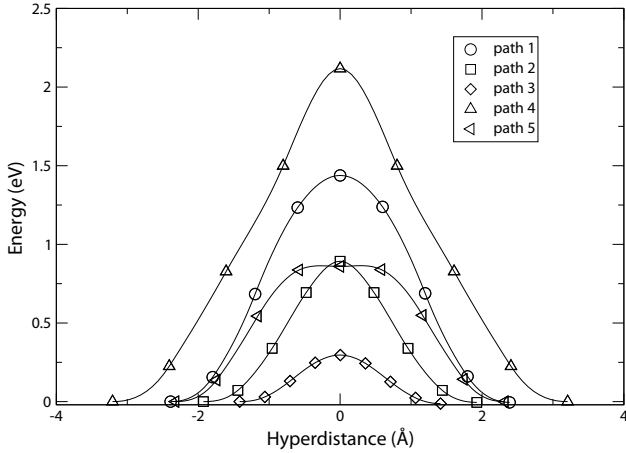


FIG. 6. Migration pathways for negative lithium vacancies along the pathways described in Table 2.

concentrations. The migration barriers for lithium vacancies were calculated for five paths, summarized in Table 2 and Figure 5. The path with the lowest barrier for negative lithium vacancies was found to be migration between symmetry distinct sites ($C \rightarrow A$), with a barrier of 0.30 eV. All other paths examined had barriers that were at least 0.5 eV higher, as shown in Figure 6.

The diffusivity can be written in terms of the defect formation and migration barriers [24]:

$$D = D_0 e^{(E_f + E_m)/kT}$$

Diffusion amongst two different types of sites is a complicated problem. However, the diffusivity does not change significantly regardless of whether migration is initiated from a TP site or from an O/T site: in both cases we find that $D = 10^{-20} \text{ m}^2/\text{s}$.

For oxygen diffusion, we consider only oxygen vacancies because they have much lower formation energies compared to the other oxygen-based defects (Table 1). The barrier to oxygen migration between sites within an O_2 dimer ($X \rightarrow W$) is only 0.26 eV. However, because this path does not provide for long range mass transport, and has a barrier much lower than all other oxygen vacancy paths examined, we treat each O_2 dimer as a single site for an oxygen vacancy for the purposes of calculating diffusivities. We calculated barriers for two other oxygen migration paths: migration

Path	Barrier (eV)
negative Li vacancy	
$C \rightarrow F$	1.44
$C \rightarrow D$	0.89
$C \rightarrow A$	0.30
$A \rightarrow E$	2.12
$A \rightarrow B$	0.86
neutral O vacancy	
$X \rightarrow W$	0.26
$X \rightarrow Z$	1.49
$X \rightarrow Y$	> 2

TABLE 2. Calculated migration barriers for defect migration.

within the basal plane ($X \rightarrow Y$) and migration between nearest sites going out of the basal plane ($X \rightarrow Z$). The path going out of the basal plane had a significantly lower barrier of 1.49 eV. Overall, we find that the oxygen diffusivity is $10^{-42} \text{ m}^2/\text{s}$, indicating that oxygen is basically immobile in Li_2O_2 .

The diffusion of defects may be a rate-limiting process in decomposition of Li_2O_2 during the recharging process. The diffusion length d represents the length scale over which diffusion occurs during a time t :

$$d = \sqrt{Dt}$$

Assuming $t = 1$ hour, based on our calculations the diffusion length is estimated to be about 10 nm. If the size of Li_2O_2 particles is significantly larger than this, decomposition may be diffusion limited. SEM studies indicate that in slowly-discharged cells ($0.2 \text{ mA}/\text{cm}^2$) the Li_2O_2 discharge product forms particles of sizes greater than 300 nm [6]. At faster discharge rates even thicker continuous films of Li_2O_2 were observed [6]. Since the dimensions of Li_2O_2 deposits are more than an order of magnitude larger than the calculated diffusion length, we predict that decomposition may be diffusion limited.

Conclusion

Density functional theory calculations have been employed to calculate the thermodynamics of Li_2O_2 surfaces, intrinsic defects, and the self diffusion rates of lithium and oxygen within bulk Li_2O_2 . From the Wulff construction, we find that the shape of Li_2O_2 is a hexagonal prism. The surface composition is predicted to consist of a minority (37%) oxygen-rich {0001} surface, with the majority of the surface area (63%) being a stoichiometric {1-100} surface. Negative lithium vacancies are found to be the dominant defect in the bulk, with a formation free energy of 0.47 eV under atmospheric conditions. Since the calculated diffusion lengths over one hour for both lithium and oxygen migration are roughly an order of magnitude smaller than the typical Li_2O_2 particle size, we conclude that slow mass transport within Li_2O_2 may contribute to the high overpotentials (and resultant low efficiencies) observed during charging.

Acknowledgements

This work was supported by the U.S. Department of Energy's *U.S.-China Clean Energy Research Center for Clean Vehicle Cooperation (CERC-CVC)*, grant no. DE-PI0000012, and by the University of Michigan-Shanghai Jiao Tong University *Collaboration on Renewable Energy Science and Technology*.

References

- [1] E.J. Cairns and P. Albertus. Batteries for electric and hybrid electric vehicles. *Ann. Rev. of Chem. and Biomol. Eng.*, 1:299–320, 2010.
- [2] U.S. Advanced Battery Consortium. Energy storage system goals.
- [3] S.D. Beattie, D.M. Manolescu, and S.L. Blair. High-capacity lithium-air cathodes. *Journal of the Electrochemical Society*, 156:A44–A47, 2009.
- [4] G. Grishkumar, B. McCloskey, A.C. Luntz, S. Swanson, and W. Wilcke. Lithium-air battery: Promise and challenges. *Journal of Physical Chemistry Letters*, 1:2193–2203, 2010.
- [5] K.M. Abraham and Z. Jiang. A polymer electrolyte-based

- rechargeable lithium/oxygen battery. *Journal of the Electrochemical Society*, 143:1–5, 1996.
- [6] J. Read. Characterization of the lithium/oxygen organic electrolyte battery. *Journal of the Electrochemical Society*, 149:A1190–A1195, 2002.
- [7] T. Ogasawara, A. DéBart, M. Holzapfel, P. Novák, and P.G. Bruce. Rechargeable Li_2O_2 electrode for lithium batteries. *Journal of the American Chemical Society*, 128:1390–1393, 2006.
- [8] Ye Xu and William A. Shelton. O_2 reduction by lithium on Au(111) and Pt(111). *Journal of Chemical Physics*, 133, 2010.
- [9] J.S. Hummelshøj, J. Blomqvist, S. Datta, T. Vegge, J. Rossmeisl, K.S. Thygesen, A.V. Luntz, K.W. Jacobsen, and J.K. Nørskov. Communications: Elementary oxygen electrode reactions in the aprotic Li-air battery. *Journal of Chemical Physics*, 132, 2010.
- [10] Y.C. Lu, Z.C. Xu, and H.A. Gasteiger et al. Platinum-gold nanoparticles: a highly active bifunctional electrocatalyst for rechargeable lithium-air batteries. *Journal of the American Chemical Society*, 132:12170–12171, 2010.
- [11] Nicola Seriani. Ab initio thermodynamics of lithium oxides: from bulk phases to nanoparticles. *Nanotechnology*, 20, 2009.
- [12] A. Débart, J. Bao, G. Armstrong, and P. Bruce. An O_2 cathode for rechargeable lithium batteries: the effect of a catalyst. *Journal of Power Sources*, 174:1177–1182, 2006.
- [13] B. Kumar, J. Kumar, R. Leese, J.P. Fellner, S.J. Rodrigues, and K.M. Abraham. A solid-state, rechargeable, long cycle life lithium-air battery. *Journal of the Electrochemical Society*, 157:A50–A54, 2010.
- [14] K. Reuter and M. Scheffler. Composition, structure, and stability of $\text{RuO}_2(110)$ as a function of oxygen pressure. *Phys. Rev. B*, 65, 2002.
- [15] A. Peles and C.G. Van de Walle. Role of charged defects and impurities in kinetics of hydrogen storage materials: a first principles study. *Physical Review B*, 76, 2007.
- [16] C.P. Flynn. *Point Defects and Diffusion*. Oxford University Press, 1972.
- [17] J.P. Perdew, K. Burke, and M. Ernzerhof. Generalized gradient approximation made simple. *Phys. Rev. Lett.*, 77:3865–3868, 1996.
- [18] P. Hohenberg and W. Kohn. Inhomogeneous electron gas. *Phys. Rev. B*, 136:B864–B871, 1964.
- [19] W. Kohn and L.J. Sham. Self-consistent equations including exchange and correlation effects. *Phys. Rev.*, 140:1133–1138, 1965.
- [20] G. Kresse and J. Furthmüller. Efficient iterative schemes for ab initio total-energy calculations using a plane-wave basis set. *Physical Review B*, 54:11169–11186, 1996.
- [21] P.E. Blöchl. Projector augmented-wave method. *Physical Review B*, 50:17953–17979, 1994.
- [22] D.C. Wallace. *Thermodynamics of Crystals*. Wiley, 1972.
- [23] H. Jónsson, G. Mills, and K.W. Jacobsen. Nudged elastic band method for finding minimum energy paths of transitions. In B.J. Berne, G. Cicotti, and D.F. Coker, editors, *Classical and quantum dynamics in condensed phase simulations*, pages 385–404. World Scientific, 1998.
- [24] S. Hao and D.S. Sholl. Hydrogen diffusion in MgH_2 and NaMgH_3 via concerted motions of charged defects. *Applied Physics Letters*, 93, 2008.
- [25] G. Wulff. On the question of speed of growth and dissolution of crystal surfaces. *Zeitschrift für Kristallographie und Mineralogie*, 34, 1901.